



Evaluation of MUSICA MetOp/IASI tropospheric water vapour profiles by theoretical error assessments and comparisons to GRUAN Vaisala RS92 measurements

Christian Borger^{1,a}, Matthias Schneider¹, Benjamin Ertl^{1,2}, Frank Hase¹, Omaira E. García³, Michael Sommer⁴, Michael Höpfner¹, Stephen A. Tjemkes⁵, and Xavier Calbet⁶

¹Institute of Meteorology and Climate Research (IMK-ASF), Karlsruhe Institute of Technology, Karlsruhe, Germany

²Steinbuch Centre for Computing (SCC), Karlsruhe Institute of Technology, Karlsruhe, Germany

³Izaña Atmospheric Research Center, Agencia Estatal de Meteorología (AEMET), Santa Cruz de Tenerife, Spain

⁴Deutscher Wetterdienst, Meteorologisches Observatorium Lindenberg, Richard-Aßmann-Observatorium, Am Observatorium 12, 15848, Lindenberg/Tauche, Germany

⁵EUMETSAT, Eumetsat Allee 1, 64295 Darmstadt, Germany

⁶AEMET, C/Leonardo Prieto Castro 8, Ciudad Universitaria, 28071 Madrid, Spain

^anow at: Satellite Remote Sensing Group, Max Planck Institute for Chemistry, Mainz, Germany

Correspondence to: C. Borger and M. Schneider

(Christian.Borger@mpic.de and matthias.schneider@kit.edu)

Abstract. Volume mixing ratio water vapour profiles have been retrieved from IASI (Infrared Atmospheric Sounding Interferometer) spectra by using the MUSICA (Multi-platform remote Sensing of Isotopologues for investigating the Cycle of Atmospheric water) processor. The retrievals are made for IASI observations that coincide with Vaisala RS92 radiosonde measurements performed in the framework of the GCOS (Global Climate Observing System) Reference Upper-Air Network (GRUAN) in three different climate zones: the tropics (Manus Island, 2°S), mid-latitudes (Lindenberg, 52°N) and polar regions (Sodankylä, 67°N).

The retrievals show good sensitivity with respect to the vertical H₂O distribution between 1–2 km above ground and the upper troposphere. Typical DOFS (degree of freedom for signal) values are about 5.5 for the tropics, 5.0 for summertime mid-latitudes, 4.0 for wintertime mid-latitudes, and 4.5 for summertime polar regions. The errors of the IASI water vapour profiles have been theoretically estimated considering the contribution of a large number of uncertainty sources. For all three climate regions unrecognized cirrus clouds and uncertainties in atmospheric temperature have been identified as the most important error sources, whereby the total errors are estimated to be typically 25%.

The IASI water vapour profiles have been compared to 100 individual coinciding GRUAN water vapour profiles. The systematic difference between the IASI and GRUAN data is within 12% at all altitudes. The scatter is largest close to the surface and close to the tropopause, but does never exceed 30%. The study documents that the MUSICA MetOp/IASI retrieval processor provides H₂O profiles with good accuracy and captures the variations in H₂O volume mixing ratio profiles from 1–2 km above ground up to altitudes close to the tropopause with a precision that is in accordance to the theoretical error assessment.



1 Introduction

Atmospheric water plays a key role for the atmospheric energy balance and temperature distribution via radiative effects (clouds and vapour) and latent heat transport. Hence the distribution and transport of atmospheric moisture is closely linked to atmospheric dynamics on all scales and understanding its spatial and temporal variations is essential for weather and climate modeling. Also, understanding the coupling between moisture transport, clouds and atmospheric dynamics is seen as a major challenge for improving atmospheric models (Stevens and Bony, 2013). In this context the global monitoring of the water vapour distribution is important, whereby the large inhomogeneity in time and space (horizontally and vertically) is particularly challenging.

In the meantime, several in situ and remote sensing measurement techniques for the observation of water vapour have been established using platforms such as surface stations, balloons, aircraft or satellites. The radiative properties of water vapour enable satellite remote sensing measurements in a large range of wavelength regimes from the visible (e.g. GOME; Grossi et al., 2015), near-infrared (e.g. MODIS; Gao and Kaufman, 2003), infrared (e.g. TES; Worden et al., 2012 and IASI; Herbin et al., 2009; Schneider and Hase, 2011) to the microwave (e.g. AMSU; Rosenkranz, 2000). The IASI instrument (Infrared Atmospheric Sounding Interferometer; Clerbaux et al., 2009) aboard EUMETSAT's MetOp satellites is particularly promising: it provides global observations with high resolution and accuracy twice a day on a long-term mission for more than 14 years. Furthermore, IASI follow-up missions have already been approved guaranteeing respective observations until the 2030s, which will offer great opportunities for studying the atmospheric composition over long time periods.

When using satellite data in research, it is important to understand their characteristics (sensitivity/representativeness and errors). Theoretical error assessments can be used to reveal the leading error sources. Ideally these error assessments should be accompanied by empirical data validation studies, in which the remote sensing data are compared to independent high quality reference data. Temperature and humidity profile reference data are produced from Vaisala RS92 radiosonde measurements in the framework of the GCOS Reference Upper-Air Network (GRUAN, www.gruan.org), a subnetwork of the Global Climate Observing System (GCOS, <http://www.wmo.int/pages/prog/gcos/index.php>). Currently GRUAN consists of about 30 reference sites.

In this paper we perform a detailed theoretical error assessment and an empirical validation of the water vapour profiles as generated by the MUSICA MetOp/IASI retrieval processor. The retrievals are made for three different climate regions (tropics, midlatitudes, polar regions) and for coincidences with GRUAN in situ radiosonde measurements, which we use as the reference for the empirical validation study. Our investigations will give a comprehensive overview of the retrieval's capability of profiling atmospheric water vapour. The paper is organised as follows: Section 2 will give a brief overview of the MUSICA MetOp/IASI processor by describing general retrieval and error estimation principles, by presenting the particularities of the MUSICA retrieval setup and by discussing the MUSICA retrieval output. Section 3 presents the sites and time periods for which the data evaluation is performed. Section 4 shows the theoretical IASI data characterisation and Sect. 5 gives the results of the comparison between the remote sensing data and the GRUAN in situ reference data. In Sect. 6 we summarize the outcome of the study.



2 MUSICA MetOp/IASI data

2.1 Atmospheric remote sensing retrieval principles

In this subsection we give a very brief introduction into the principles of the optimal estimation retrieval method. It is a standard retrieval method in atmospheric remote sensing. For more details please refer to Rodgers (2000) and for a general introduction on vector and matrix algebra dedicated textbooks are recommended.

Atmospheric remote sensing means that the atmospheric state is retrieved from the radiation measured after having interacted with the atmosphere. This interaction of radiation with the atmosphere is modeled by a radiative transfer model (also called forward model, F), which enables relating the measurement vector and the atmospheric state vector by:

$$\mathbf{y} = F(\mathbf{x}, \mathbf{p}) \quad (1)$$

We measure \mathbf{y} (the measurement vector, e.g. a thermal nadir spectrum in the case of IASI) and are interested in \mathbf{x} (the atmospheric state vector). Vector \mathbf{p} represents auxiliary parameters (like surface emissivity) or instrumental characteristics (like the instrumental line shape), which are not part of the retrieval state vector. However, a direct inversion of Eq. (1) is generally not possible, because there are many atmospheric states \mathbf{x} that can explain one and the same measurement \mathbf{y} .

For solving this ill-posed problem a cost function is set up, that combines the information provided by the measurement with a priori known characteristics of the atmospheric state:

$$[\mathbf{y} - F(\mathbf{x}, \mathbf{p})]^T \mathbf{S}_\epsilon^{-1} [\mathbf{y} - F(\mathbf{x}, \mathbf{p})] + [\mathbf{x} - \mathbf{x}_a]^T \mathbf{S}_a^{-1} [\mathbf{x} - \mathbf{x}_a]. \quad (2)$$

Here, the first term is a measure of the difference between the measured spectrum (represented by \mathbf{y}) and the spectrum simulated for a given atmospheric state (represented by \mathbf{x}), while taking into account the actual measurement noise level (\mathbf{S}_ϵ is the measurement noise covariance matrix). The second term of the cost function (Eq. 2) constrains the atmospheric solution state (\mathbf{x}) towards an a priori most likely state (\mathbf{x}_a), whereby kind and strength of the constraint are defined by the a priori covariance matrix \mathbf{S}_a . The constrained solution is reached at the minimum of the cost function (Eq. 2). Due to the nonlinear behavior of $F(\mathbf{x}, \mathbf{p})$, the minimisation is generally achieved iteratively. For the $(i + 1)$ th iteration it is:

$$\mathbf{x}_{i+1} = \mathbf{x}_a + \mathbf{G}_i [\mathbf{y} - F(\mathbf{x}_i, \mathbf{p}) + \mathbf{K}_i (\mathbf{x}_i - \mathbf{x}_a)]. \quad (3)$$

\mathbf{K} is the Jacobian matrix (derivatives that capture how the measurement vector will change for changes in the atmospheric state \mathbf{x}). \mathbf{G} is the gain matrix (derivatives that capture how the retrieved state vector will change for changes in the measurement vector \mathbf{y}). \mathbf{G} can be calculated from \mathbf{K} , \mathbf{S}_ϵ and \mathbf{S}_a as:

$$\mathbf{G} = (\mathbf{K}^T \mathbf{S}_\epsilon^{-1} \mathbf{K} + \mathbf{S}_a^{-1})^{-1} \mathbf{K}^T \mathbf{S}_\epsilon^{-1}. \quad (4)$$

The averaging kernel is an important component of a remote sensing retrieval and it is calculated as:

$$\mathbf{A} = \mathbf{GK}. \quad (5)$$



The averaging kernel \mathbf{A} reveals how a small change of the real atmospheric state vector \mathbf{x} affects the retrieved atmospheric state vector $\hat{\mathbf{x}}$:

$$\hat{\mathbf{x}} - \mathbf{x}_a = \mathbf{A}(\mathbf{x} - \mathbf{x}_a). \quad (6)$$

The propagation of errors due to parameter uncertainties ϵ_p can be estimated analytically with the help of the parameter Jacobian matrix \mathbf{K}_p (derivatives that capture how the measurement vector will change for changes in the parameter p). According to Eq. (3), using the parameter $p + \epsilon_p$ (instead of the correct parameter p) for the forward model calculations will result in an error in the atmospheric state vector of:

$$\mathbf{x}_e = -\mathbf{G}\mathbf{K}_p\epsilon_p. \quad (7)$$

The respective error covariance matrix \mathbf{S}_e is:

$$\mathbf{S}_e = \mathbf{G}\mathbf{K}_p\mathbf{S}_p\mathbf{K}_p^T\mathbf{G}^T, \quad (8)$$

where \mathbf{S}_p is the covariance matrix of the uncertainties ϵ_p .

Noise on the measured radiances also affects the retrievals. The error covariance matrix for noise can be analytically calculated as:

$$\mathbf{S}_e = \mathbf{G}\mathbf{S}_y\mathbf{G}^T, \quad (9)$$

where \mathbf{S}_y is the covariance matrix for noise on the measured radiances \mathbf{y} .

2.2 The MUSICA retrieval setup

The MUSICA MetOp/IASI retrieval is based on a nadir version of the retrieval code PROFFIT (PROFile FIT; Hase et al., 2004) and on the corresponding radiative transfer model PRFFWD (PRoFit ForWarD model; Hase et al., 2004). The nadir code has been developed in support of the project MUSICA (MUlti-platform remote Sensing of Isotopologues for investigating the Cycle of Atmospheric water, <http://www.imk-asf.kit.edu/english/musica.php>). The PRFFWD-nadir code has been recently updated by including water continuum calculations according to the model “MT_CKD” v2.5.2 (Mlawer et al., 2012; Delamere et al., 2010; Payne et al., 2011).

For the MUSICA MetOp/IASI retrieval calculations a single broad spectral window ranging from 1190 cm^{-1} to 1400 cm^{-1} is used. The spectral signatures of H_2^{16}O , H_2^{18}O and H_2^{17}O are fitted together as a single species and HDO as a separate species. Furthermore, the retrieval’s spectral window contains spectroscopic features of CH_4 and N_2O as well as weak spectroscopic features of HNO_3 and very weak spectroscopic features of CO_2 and O_3 . All these trace gases (except O_3) are simultaneously fitted during the retrieval process whereby the spectroscopic parameters are taken from the HITRAN database (Gordon et al., 2017) with small modifications for HDO parameters (similar to Schneider et al., 2016, the line intensity parameters of HDO have been increased by 10%).



The water isotopologues are retrieved on a logarithmic scale. For CO_2 and HNO_3 the a priori profiles are scaled and for CH_4 and N_2O an ad hoc regularisation is applied allowing profile retrievals on a logarithmic scale (García et al., 2017). A single a priori is used for all the retrievals for each of the different trace gases (Schneider et al., 2016; García et al., 2017).

The retrieval also fits the surface temperature and the atmospheric temperature profile, whereby the a priori temperatures are taken from the EUMETSAT IASI level 2 (L2) products. There is no constraint on the surface temperature. The allowed atmospheric temperature variations are 1 K at ground, 0.5 K in the free troposphere, and 0.75 K above the tropopause. This altitude dependency follows roughly the altitude dependency of uncertainties in the EUMETSAT IASI L2 atmospheric temperature profiles (August et al., 2012).

The MUSICA MetOp/IASI water vapour retrieval only works for pixels that are not contaminated by clouds, whereby we rely on the IASI L2 cloud flag (we require zero for the flag “cldfrm”). Ground elevations are from GTOPO30 developed by US Geological Survey and provided by the Oak Ridge National Laboratory Distributed Active Archive Center (ORNL DAAC). GTOPO30 is a global digital elevation model with a horizontal grid spacing of 30-arc seconds (approximately 1 km). The land surface emissivities are from the “global database of infrared land surface emissivity” (IREMIS; <http://cimss.ssec.wisc.edu/iremisk/>; Seemann et al., 2008) and the sea surface emissivities are calculated according to the model of Masuda et al. (1988).

Figure 1 depicts an example of a typical radiance spectrum in the retrieval’s spectral range as measured by IASI (upper graph) and the corresponding differences to the simulated spectra (the residuals, lower graph). The residuals are mostly within the order of the instrument’s 1σ measurement noise (Pequignot et al., 2008). However, there are also distinctive spectral signatures that are not well understood, specifically at 1250 cm^{-1} and at 1280 cm^{-1} .

For further information on the retrieval setup a more detailed description is available in Schneider and Hase (2011) and Wiegele et al. (2014).

2.3 The MUSICA retrieval output

The output of the retrieval refers to the $\{\ln[\text{H}_2\text{O}], \ln[\text{HDO}]\}$ basis system. In this basis system the state vector \mathbf{x} consists of the vector for the H_2O profile extended by the vector for the HDO profile:

$$\mathbf{x} = \begin{pmatrix} \mathbf{x}_{\text{H}_2\text{O}} \\ \mathbf{x}_{\text{HDO}} \end{pmatrix}. \quad (10)$$

Correspondingly, the averaging kernel matrix \mathbf{A} has 2×2 blocks

$$\mathbf{A} = \begin{pmatrix} \mathbf{A}_{11} & \mathbf{A}_{12} \\ \mathbf{A}_{21} & \mathbf{A}_{22} \end{pmatrix}. \quad (11)$$

\mathbf{A}_{11} and \mathbf{A}_{22} describe how the retrieved H_2O and HDO states depend on the actual atmospheric H_2O and HDO variations, respectively, and \mathbf{A}_{12} and \mathbf{A}_{21} reveal the cross-dependencies of the retrieved H_2O on the actual atmospheric HDO and of the retrieved HDO on the actual atmospheric H_2O , respectively. Since H_2O and HDO vary largely in parallel, we use in the following the $\mathbf{A}_{11} + \mathbf{A}_{12}$ as the kernel for H_2O (see also Sect. 4.3 in Barthlott et al., 2017).



Similarly, retrieval error covariance matrices consist of 2×2 blocks where the blocks in the diagonal represent the H₂O and HDO covariances. For this study only the H₂O covariance block is of interest (i.e. we are only interested in the H₂O error covariances). The outer diagonal blocks represent the error covariances between H₂O and HDO.

3 Reference data and sites

5 The theoretical and empirical assessment studies are made for cloud-free IASI measurements that coincide with GRUAN processed Vaisala RS92 radiosonde measurements. Useful coincidences are defined in accordance to Pougatchev et al. (2009) and Calbet et al. (2017).

We identified three different sites with coincidence between IASI and GRUAN measurements: Manus Island (Papua New Guinea; 2°5'S, 146°58'E) for the tropics, Lindenberg (Germany; 52°12'N, 14°7'E) for the mid-latitudes and Sodankylä (Fin-
10 land; 67°25'N, 26°35'E) for the polar region.

Figure 2 depicts all the GRUAN H₂O profiles that coincide with IASI observation made for cloud-free conditions. There are 25 individual GRUAN profiles for Manus Island, 58 for Lindenberg, and 17 for Sodankylä, i.e. in total there are 100 individual GRUAN radiosonde measurements that coincide with IASI cloud-free measurements. This ensemble of GRUAN profiles is well representative for the highly varying tropospheric H₂O distributions. In the free middle/upper troposphere the data show
15 variations of up to two orders of magnitude. At the tropical site of Manus Island we observe up to 10 000 ppmv (at 5 km a.s.l.) and up to 1000 ppmv (at 10 km a.s.l.), whereas at the mid-latitudinal and polar sites of Lindenberg and Sodankylä the H₂O concentrations can be as small as 100 ppmv and 10 ppmv, respectively. In this context using this ensemble of GRUAN data enables us to make an evaluation of the retrieval performance that has a good global validity.

The coincidences at the three sites are for different time periods meaning that there is not a strictly uniform data set for
20 creating the retrieval input files (more details see Sects. 3.2-3.4 and the summary of Table 1).

3.1 GRUAN processed Vaisala RS92 in-situ profiles

The Vaisala RS92 radiosonde is equipped with a wire-like capacitive temperature sensor (“Thermocap”), two polymer capacitive moisture sensors (“Humicap”), a silicon-based pressure sensor and a GPS receiver to measure position, altitude and winds. Each second the RS92 transmits sensor data, which are received, processed and stored by the ground station equipment.

25 The Humicap consists of a hydro-active polymer thin film as dielectric between two electrodes applied on a glass substrate. The humidity sensors are not covered by protective caps, but they are alternately heated to prevent icing. To prevent overheating, the heating of the humidity sensors is switched off below −60 °C, or above 100 hPa, whichever is reached first. Humicaps show good performance over a wide range of temperatures but suffer from systematic errors such as dry bias due to solar radiative heating and a response lag below −40 °C. Known main error sources affecting the humidity profile are daytime solar heat-
30 ing of the Humicaps introducing a dry bias, sensor time-lag at temperatures below about −40 °C and temperature-dependent calibration correction.



We work with Vaisala RS92 data that have been processed by the GRUAN lead centre (<http://www.gruan.org>). The GRUAN data processing assures that the obtained humidity, pressure and temperature profiles are well-calibrated and highly accurate (Dirksen et al., 2014; Sommer et al., 2016).

3.2 Manus Island (MI)

5 At Manus Island we have coincidences in 2012 and 2013 to 25 individual GRUAN radiosonde profiles. The collocation of IASI and GRUAN measurements has been performed by EUMETSAT in the framework of a planned IASI retrieval comparison study (Calbet et al., 2017).

For our retrieval we use the a priori temperatures (atmosphere and surface skin) as well as surface emissivities from the EUMETSAT IASI L2 product. Since most of the ground scenes are over the ocean surface, the emissivity values are mainly
10 according to the model of Masuda et al. (1988). The satellite pixels have been carefully examined for clouds by EUMETSAT according to the cloud flags as provided in the IASI L2 data.

3.3 Lindenberg 2008 (LI08)

For Lindenberg there are coincidences to 32 individual GRUAN profiles in 2008 (representative for all seasons). We performed the collocation and required that the satellite pixel has to be within a distance of 25 km with respect to the starting position of
15 the radiosonde and that the satellite's pixel sensing time has to be within the sensing time period of the radiosonde.

Like for Manus Island we rely on the IASI L2 data for our retrieval input data (surface and atmospheric temperatures, surface emissivity, cloud filter, etc.). However, while for the 2012/13 time period (Manus Island) the IASI L2 data are generated with the IASI L2 PPF (Product Processing Facility) software version 5, for the 2008 retrievals we work with L2 data generated by the IASI L2 PPF software version 4.

20 3.4 Lindenberg 2007 (LI07) and Sodankylä 2007 (SK07)

In 2007 we have 26 individual GRUAN profiles for Lindenberg and 17 individual GRUAN profiles for Sodankylä (details on the Sodankylä campaign are available in Calbet et al., 2011) that coincide with IASI observations. This dataset is limited to the summer observations. We performed the collocation using the same criteria as for the Lindenberg 2008 coincidences.

For summer 2007 IASI L2 data have not been available for our retrieval input. Thus data from the radiosonde measurements
25 have been used as the a priori temperatures and this might cause some minor inconsistencies to a retrieval that uses IASI L2 temperatures as a priori temperature (the MI and LI08 retrievals). Surface emissivities are taken from the "global database of infrared land surface emissivity" (IREMIS; <http://cimss.ssec.wisc.edu/iremisp/>; Seemann et al., 2008), i.e. in agreement to the retrievals for 2008 (IASI L2 emissivities are based on IREMIS for land surfaces and use the Masuda model for sea surfaces). Because there are no IASI L2 cloud products for summer 2007, we use the radiosonde measurements and the cloud detection
30 algorithm according to the model of Zhang et al. (2010) for identifying cloud-free situations.



4 Theoretical MUSICA MetOp/IASI data characterisation

4.1 Averaging Kernels

Figure 3 illustrates examples of H₂O row kernels ($\mathbf{A}_{11} + \mathbf{A}_{12}$, logarithmic state vector entries according to Sect. 2.3) for the three reference sites. The peaks of the row kernels for the heights of 1.8 km, 4.9 km, 8.0 km and 10.9 km are close to their nominal altitudes, meaning that the values retrieved for this altitudes well represent the situation at the nominal altitude. In contrast the row kernel for the lowermost troposphere (kernel with 0.4 km nominal altitude) peaks at around 1 km at every reference site and is not well separated from the row kernels with nominal altitudes just above the boundary layer (kernel with 1.2 km nominal altitude). This shows that the retrieval has a poor sensitivity for the atmospheric layers near the ground.

For higher altitudes the sensitivity is best in the tropics and poorest in the polar region. In agreement with the location of the tropopause we observe good sensitivity in the tropics up to 13 km, in mid-latitudes up to 11-12 km in summer and 8 km in winter and in polar regions in up to 11 km in summer. This becomes evident by looking on the altitudes where the example kernels of Fig. 3 have their peak levels. Whereas for Manus Island the 13.6 km kernel is the uppermost kernel that peaks close to its nominal altitude, for Lindenberg and Sodankylä the respective kernels are the 10.9 km kernels.

The seasonal dependency of the sensitivity is indicated in Fig. 5, which depicts the seasonal variations in the degree of freedom for signal (DOFS) values. The DOFS values are calculated as the trace of the averaging kernel matrix and the higher the DOFS values the more profile information is in the retrieved atmospheric state. In the tropics we observe no seasonal dependency. In the mid-latitudes the DOFS values are distinctively higher in summer than in winter (for polar regions we analyse only summertime observations). The seasonal variations in the mid-latitudes are in line with the seasonal variation of the tropopause.

In summary, at all three different sites the MUSICA MetOp/IASI retrieval provides H₂O profile information from 1.5–2 km above ground up to about the tropopause altitude.

4.2 Calculation of error Jacobians

The error Jacobians ($\mathbf{K}_{\mathbf{p}}$ from Eqs. 7 and 8) are calculated by the forward model PRFFWD (Hase et al., 2004) as follows: PRFFWD is executed running on a vertical grid of 28 levels from surface altitude to approximately 55 km above mean sea level. For every site reference forward calculations are performed for all cloud-free situations. The input (i.e. temperature, trace gas concentrations, etc.) for the reference forward model runs is the same as the input used in the forward calculation of the last iteration step of the MUSICA MetOp/IASI retrievals, i.e. the reference radiances are given by $\mathbf{F}(\hat{\mathbf{x}}, \mathbf{p})$. Then for each reference scenario we make additional forward calculations with slightly modified parameters, i.e. we calculate $\mathbf{F}(\hat{\mathbf{x}}, \mathbf{p} + \varepsilon_p)$. For a measurement vector \mathbf{y} having m elements and a parameter vector \mathbf{p} having n elements the Jacobian matrix $\mathbf{K}_{\mathbf{p}}$ will have the dimension $m \times n$. The individual matrix elements are calculated as:

$$\mathbf{K}_{\mathbf{p}_{k,1}} = \frac{F_k(\hat{\mathbf{x}}, \mathbf{p} + \varepsilon_{p_i}) - F_k(\hat{\mathbf{x}}, \mathbf{p})}{\varepsilon_{p_i}}, \quad (12)$$



where k is the index for the k th element of the measurement state vector \mathbf{y} (simulated by vector function F) and l is the index for the l th element of the parameter vector \mathbf{p} , respectively.

Table 2 gives an overview of the uncertainty assumptions ε_p used for calculating the Jacobians and for performing the error estimation. The calculations of the error Jacobians for water vapour continuum and clouds require a specific treatment, which is detailed in the following two subsections.

4.2.1 Water vapour continuum

We hypothetically assume that calculations based on the model “MT_CKD” v2.5.2 (Mlawer et al., 2012; Delamere et al., 2010; Payne et al., 2011) only partly capture the full water vapour continuum effect. For the respective Jacobian calculation we perform forward calculations without considering the water vapour continuum ($F_{\text{noWVC}}(\hat{\mathbf{x}}, \mathbf{p})$). Then we calculate the Jacobian matrix as $\mathbf{K}_{\text{noWVC}} = F_{\text{noWVC}}(\hat{\mathbf{x}}, \mathbf{p}) - F(\hat{\mathbf{x}}, \mathbf{p})$. The spectral response for an underestimation of 10% of the water vapour continuum effect is then $\mathbf{K}_{\text{noWVC}}\varepsilon_{\text{noWVC}}$ with $\varepsilon_{\text{noWVC}} = 0.1$.

4.2.2 Opaque clouds (cumulus)

We estimate the influence of fractional coverage with opaque liquid cumulus clouds with different cloud top altitudes (1.3 km, 3.0 km and 4.9 km). The radiance at top of the cloudy atmosphere $F_{\text{cum}}(\hat{\mathbf{x}}, \mathbf{p})$ is calculated by starting PRFFWD at the cloud’s top height, assuring that no radiation from below the cloud contributes to $F_{\text{cum}}(\hat{\mathbf{x}}, \mathbf{p})$. Additionally it is assumed that the surface emissivity of the cloud is 1.0 and that the skin temperature of the cloud’s upward looking surface is in thermal equilibrium with the surrounding air temperature. The Jacobian matrix for opaque cumulus clouds is then $\mathbf{K}_{\text{cum}} = F_{\text{cum}}(\hat{\mathbf{x}}, \mathbf{p}) - F(\hat{\mathbf{x}}, \mathbf{p})$ and the spectral response of a 10% fractional cloud cover is $\mathbf{K}_{\text{cum}}\varepsilon_{\text{cum}}$ with $\varepsilon_{\text{cum}} = 0.1$.

4.2.3 Transmitting clouds (mineral dust and cirrus)

Some clouds are not opaque and we have to consider partial attenuation by the cloud particles. This is the case for cirrus clouds and mineral dust clouds. We consider these clouds by introducing them as an additional species in the forward model calculations. The extinction of these clouds is the sum of absorption and scattering. Since PRFFWD does not include the simulation of scattering clouds we calculate the attenuated radiances using forward model calculations from KOPRA (Karlsruhe optimized and precise radiative transfer algorithm; Stiller, 2000) and consider single scattering.

The frequency dependency of the extinction cross sections, the single scattering albedo, and the scattering phase functions of the clouds are calculated from OPAC v4.0b (Optical Properties of Aerosol and Clouds; Hess et al., 1998; Koepke et al., 2015). For cirrus clouds we assume the particle composition as given by OPAC’s “Cirrus 3” ice cloud example (see Table 1b in Hess et al., 1998) and for mineral dust clouds a particle composition according to OPAC’s “Desert” aerosol composition example (see table Table 4 in Hess et al., 1998).



We make cirrus cloud forward calculations F_{cir} considering cirrus clouds with a vertical cloud layer thickness of 1 km and cloud top at different altitudes ranging from 6 km to 14 km. The Jacobians are calculated as $K_{\text{cir}} = F_{\text{cir}}(\hat{x}, p) - F(\hat{x}, p)$ and for a cloud coverage of 50% the spectral response is $K_{\text{cir}}\varepsilon_{\text{cir}}$ with $\varepsilon_{\text{cir}} = 0.5$.

For the dust clouds we make forward calculations F_{dust} for homogeneous 2 km thick layers between the ground and 6 km altitude. The Jacobians are then given as $K_{\text{dust}} = F_{\text{dust}}(\hat{x}, p) - F(\hat{x}, p)$.

4.3 Spectral response on uncertainty

Figure 5 depicts the spectral responses (i.e. $K_p\varepsilon_p$) for an example of different uncertainty sources for a typical situation at the tropical reference site. The left panel shows that surface skin temperature uncertainties mainly affect the spectra between 1190 cm^{-1} to 1250 cm^{-1} (which is also the spectral region of an “atmospheric window”), but is negligible for higher wavenumbers. This is similar for lower tropospheric temperature uncertainties and in contrast to upper tropospheric temperature uncertainties, which have highest spectral responses for wavenumbers larger than 1250 cm^{-1} .

The right panel of Fig. 5 illustrates that uncertainties in dust layers and uncertainties due to cirrus clouds have the highest impact at the lower end of wavenumbers and that a cirrus cloud has a weaker dependency on wavenumber than a dust layer. Furthermore unrecognized clouds have the opposite effect on the spectrum than increasing the surface skin and atmospheric temperatures although affecting the spectrum in the same order of magnitude.

4.4 Estimated errors

Figure 4 shows a certain seasonal variability in the DOFS values (in particular at the mid-latitudinal site), indicating varying sensitivities of the remote sensing system. This variation is also present in the sensitivity with respect to uncertainty sources. For this reason we present the estimated errors for all the Manus Island and Sodankylä retrievals and for all the Lindenberg 2008 retrievals. The Lindenberg 2008 error estimations are representative for all seasons, hence they cover the full variation with respect to uncertainty sources.

4.4.1 Measurement noise

Figure 6 depicts the H_2O error profiles for noise on the measured radiances (from the left to the right for Manus Island, Lindenberg, and Sodankylä). The shown error profiles are the square root of the diagonal elements of the error covariance matrix S_e calculated according to Eq. (9). For these calculations we assume a noise covariance S_e of the IASI radiances according to Pequignot et al. (2008).

The measurement noise errors vary around 2-10% near the ground but decrease to approximately 2-3% above the boundary layer and remain there throughout the free troposphere. Above and close to the tropopause errors increase again to values of around 10%. For Manus Island we observe similar errors for all the different observations. For Sodankylä and in particular for Lindenberg the errors vary. For instance, in the lower troposphere at Lindenberg the error is 10% for some days, but only 1-3%



for other days. The varying sensitivity with respect to the uncertainty sources is due to the varying atmospheric conditions and in agreement with the varying DOFS values as documented by Fig. 4 (the Lindenberg data cover all mid-latitude seasons).

4.4.2 Temperature and surface emissivity

The H₂O error pattern profiles due to positive errors in surface emissivity, surface skin temperature and atmospheric temperatures are calculated as x_e according to Eq. (7). The patterns are plotted in Fig. 7 (top panels for uncertainties in surface emissivity and surface skin temperature and bottom panels for uncertainties in atmospheric temperatures).

Uncertainties in the surface emissivity of +2% have a strong impact near the ground (errors of approx. 20-40%). For Manus Island, the error is always negative in the lower troposphere and similar for all observations, whereas for Lindenberg and Sodankylä a +2% uncertainty in the surface emissivity causes sometimes positive and sometimes negative errors in the lower troposphere, i.e. the sensitivity with respect to this uncertainty source is strongly varying. Surface skin temperature is fitted during the retrieval process, i.e. uncertainties in the first guess surface skin temperatures are partly corrected for during the retrieval process. The remaining error due to an +2 K surface skin temperature uncertainty is largest in the lower troposphere, where it can reach up to 20%. It can be positive or negative. Above 4 km altitude the surface emissivity and surface skin temperature uncertainties are smaller than 5%.

Positive atmospheric temperature uncertainties cause large positive errors in the retrieved tropospheric H₂O profiles. The errors can reach +30%, whereby these errors are largest for the heights (and atmospheric layers respectively) where the atmospheric temperature uncertainty is assumed: for instance, uncertainties in lower tropospheric temperature (0-2 km, upper row) cause maximal errors from ground up to 3 km and decrease rapidly with altitude onwards, whereas uncertainties in upper tropospheric temperature (5-10 km, bottom row) are negligible from ground up to 6 km, but then increase to values of around +20% at 8 km.

4.4.3 Spectroscopic parameters

Figure 8 illustrates the error pattern profiles (x_e according to Eq. 7) for uncertainties in the spectroscopic parameters. We consider uncertainties in the H₂O line intensity and pressure broadening parameters and an uncertainty in the applied water continuum model.

The uncertainty in the water vapour continuum model causes error profiles having small oscillations. For a water continuum model that underestimates the water continuum effect by 10% (see Sect. 4.2.1), the error is positive near ground (about +2%), negative at around 3 km altitude (about -4%) and negligible for altitudes above 5 km.

A positive uncertainty of +5% in the linestrength parameter causes a negative error of about -5% in the retrieved H₂O values, with slight oscillations (the slight oscillation is an effect of the constraint between H₂O and HDO applied for the MUSICA retrievals). The impact of uncertainties in the pressure broadening parameter depends on the reference site: At Manus Island the resulting errors are negligible above 3 km, but at Lindenberg and Sodankylä the error profiles contain strong oscillations with an amplitude of approximately 10% and maximal errors close to the tropopause.



Uncertainties in the spectroscopic parameters of HDO and due to varying CH₄ and N₂O concentrations account for absolute error values of less than 1% and are not depicted in the Figure.

4.4.4 Clouds

Figure 9 shows the influence of different cloud types on the retrieval. Uncertainties due to unrecognized cirrus clouds (top row in Fig. 9) lead to errors of -20% from 3-6 km at all sites and then decrease with altitude. However their impact on the humidity profiles in the boundary layer shows large variation, especially at Lindenberg and Sodankylä, which is a result of the more variable atmospheric conditions at these sites (compared to the tropical site of Manus Island).

The influence of a 10% fractional cloud cover of opaque clouds depends on the height where the clouds are assumed (middle row in Fig. 9): Clouds at 1.3 km show only a small impact on the humidity profiles in the boundary layer with error magnitudes of 5-10%, but clouds at 3.0 km account for errors of more than 10% up to 5 km above mean sea level. Yet similarly to cirrus clouds their effect in the boundary layer shows large variation at Lindenberg and Sodankylä.

The error pattern profiles due to mineral dust layers (bottom row in Fig. 9) show that such layers have almost no impact if they are situated in the boundary layer, however if they are situated in the middle troposphere the errors can account for values of more than 10%. The effect of dust clouds can be in particular large for the mid-latitudinal site of Lindenberg, where we also observe the largest variability in the calculated error patterns.

5 Empirical validation study

We use GRUAN processed Vaisala RS92 radiosonde measurements as reference for empirically validating the retrieved IASI H₂O profiles. The radiosonde ascents are collocated temporally and spatially with MetOp overpasses (details see Sect. 3), which is essential for a meaningful comparison.

5.1 Regridding and smoothing of high resolution in-situ profiles

The in situ profiles have a high vertical resolution. This is different to the remote sensing profiles, which can only detect the major characteristics of the vertical H₂O distribution. Before comparing the data we have to account for this different characteristics by regridding and smoothing the in situ profiles.

While the remote sensing retrieval provides atmospheric states and averaging kernels on a coarse atmospheric grid (between ground level and about 55 km a.s.l. 28 grid points are defined), the radiosonde reports data about every 10 m. So we have to regrid the radiosonde data to the coarse vertical grid used by the remote sensing retrieval. In order to guarantee that the regridding does not significantly affect the H₂O partial columns, the regridding is performed in two steps.

First, the radiosonde data points between the 28 MUSICA retrieval grid points are averaged by using a triangle inverse-distance weighted function resulting in a first estimate of the regridded radiosonde data. In the second step this first estimate is corrected by requiring that the partial columns between adjacent grid levels remain almost the same in the original high resolution data and in the regridded data. In the correction process a constraint is put to the smoothness of the profile, thereby



avoiding that the correction produces strongly oscillating profiles. The results are regrided data consisting of reasonably smooth profiles having practically the same partial columns as the original high resolved radiosonde profiles.

In order to get the in situ profile data that are comparable to the remote sensing data we have to smooth the regrided in situ profiles $\mathbf{x}_{\text{GRUAN}}$ according to the averaging kernels of the remote sensing retrieval. The regrided and smoothed in situ profile

5 $\hat{\mathbf{x}}_{\text{GRUAN}}$ is then comparable to the remote sensing profile, whereby:

$$\hat{\mathbf{x}}_{\text{GRUAN}} = (\mathbf{A}_{11} + \mathbf{A}_{12})(\mathbf{x}_{\text{GRUAN}} - \mathbf{x}_a) + \mathbf{x}_a. \quad (13)$$

Here \mathbf{A}_{11} is the H₂O block of the averaging kernel matrix and \mathbf{A}_{12} the block that describes the response of the retrieved H₂O on atmospheric HDO (see Sect. 2.3) and the vector \mathbf{x}_a is the a priori state vector. An example illustrating the effects of the regriding and the smoothing is given in Fig. 10.

10 We would like to note that by using Eq. (13) we assume that H₂O and HDO variations are fully correlated. However, H₂O and HDO do not vary fully in parallel, i.e. calculating $\hat{\mathbf{x}}_{\text{GRUAN}}$ according to Eq. (13) implies an uncertainty that can be estimated by the uncertainty covariance matrix $\mathbf{S}_{\text{e,GRUAN}}$ according to (see also Sect. 4.3 of Barthlott et al., 2017):

$$\mathbf{S}_{\text{e,GRUAN}} = \mathbf{A}_{12} \mathbf{S}_{\text{a},\delta\text{D}} \mathbf{A}_{12}^T. \quad (14)$$

15 Here $\mathbf{S}_{\text{a},\delta\text{D}}$ describes the actual atmospheric δD covariances. Because \mathbf{A}_{12} and $\mathbf{S}_{\text{a},\delta\text{D}}$ have small entries only, this uncertainty is below 1% and can be neglected for our comparison.

5.2 Comparison of GRUAN and IASI data

In this section we present the comparison between the regrided and smoothed GRUAN H₂O profiles and the IASI H₂O profiles. Thereby we illustrate the remote sensing data quality at the three reference sites that belong to three different climate zones. It should be noted that the radiosonde measurements are also affected by several uncertainties which have to be taken
 20 into account during the evaluation.

In general the uncertainty of the GRUAN data increases with altitude. For the regrided and smoothed GRUAN profiles it is about 3-5% near the surface and 5-20% at around 10 km altitude. For further information on the radiosonde uncertainty we refer to Appendix A.

5.2.1 Correlation plots

25 We use scatter plots for representing the results at selected heights where the retrieval has a good sensitivity at the respective reference sites. Figure 11 illustrates correlations between the retrieval results and the smoothed GRUAN data for selected retrieval altitude levels representative for the lower, middle and upper troposphere, respectively. For the lower and middle troposphere we use the same altitude levels (1.8 km and 4.9 km, respectively) at all reference sites. For the upper troposphere we illustrate the values for the highest altitude level at which the row kernels in Fig. 3 still indicate good sensitivity. This is
 30 about 13.5 km for Manus Island and about 11 km for Lindenberg and Sodankylä.

Near the ground and in the lower troposphere (top row in Fig. 11) the retrieval has a slightly higher variability than the radiosonde measurements for the sites of Manus Island and Sodankylä, however the remote sensing and the in situ data well



identify whether the air is more humid or drier than given by the a priori assumption (represented by the yellow star). For Lindenberg we observe two outliers in the LI08 data, which might indicate the observation of different airmasses by IASI and GRUAN.

In the middle troposphere (middle row of Fig. 11) the retrieval and the measurements remain in quasi-linear relation over nearly one order of magnitude at all reference sites. This indicates the good sensitivity and precision of the remote sensing data at this altitude region.

In the upper troposphere close to the tropopause (bottom row) the H₂O variability at Manus Island is rather small. In agreement to the GRUAN radiosonde, the retrieval estimates an H₂O increase if compared to the a priori assumption. It should also be noted that the concentrations at this altitude are rather low (10–40 ppmv) compared to the concentrations near the ground (about 20 000 ppmv at 1.8 km). At Lindenberg and Sodankylä the H₂O variability is higher and well captured by the IASI retrieval, despite the small humidity levels of below 100 ppmv.

The error bars on the diagonal of the plots of Fig. 11 indicate the typical GRUAN errors ($\hat{x}_{e,GRUAN}$ as detailed in Appendix A) and the root square sum of the typical leading statistical IASI errors (x_e from Eq. 7), whereby we have considered measurement noise and uncertainties in surface emissivity, surface skin temperatures and atmospheric temperatures.

5.2.2 Bias and scatter

For a better statistical quantification of the deviations of the remote sensing data from the GRUAN reference data, we introduce a skill score DL describing the difference of the logarithmic values of the respective water vapour concentrations:

$$DL = \ln([H_2O]_{\text{retrieval}}) - \ln([H_2O]_{\text{GRUAN}}) \approx \frac{[H_2O]_{\text{retrieval}} - [H_2O]_{\text{GRUAN}}}{[H_2O]_{\text{GRUAN}}}, \quad (15)$$

where $[H_2O]_{\text{GRUAN}}$ is the regridded and smoothed radiosonde H₂O data (i.e. \hat{x}_{GRUAN} from Eq. 13) and $[H_2O]_{\text{retrieval}}$ is the retrieved IASI H₂O data. The so defined skill score DL is a good measure for the relative difference between the GRUAN and IASI data.

As a good measure for the mean relative difference between GRUAN and IASI we can use the mean difference of logarithmic values (MDL):

$$MDL = \frac{1}{N} \sum_{i=1}^N DL_i = \frac{1}{N} \sum_{i=1}^N [\ln([H_2O]_{\text{retrieval}}) - \ln([H_2O]_{\text{GRUAN}})]_i \approx \frac{1}{N} \sum_{i=1}^N \left(\frac{[H_2O]_{\text{retrieval}} - [H_2O]_{\text{GRUAN}}}{[H_2O]_{\text{GRUAN}}} \right)_i. \quad (16)$$

Similarly, we can use the standard deviation of the logarithmic differences as a measure for the relative scatter between GRUAN and IASI and introduce σ_{MDL} as

$$\sigma_{MDL} = \sqrt{\frac{1}{N} \sum_{i=1}^N (DL_i - MDL)^2}. \quad (17)$$



For illustrating the variation of the atmospheric state we introduce σ_{GRUAN} as

$$\sigma_{\text{GRUAN}} = \sqrt{\frac{1}{N} \sum_{i=1}^N \left[\ln([\text{H}_2\text{O}]_{\text{GRUAN}})_i - \overline{\ln([\text{H}_2\text{O}]_{\text{GRUAN}})} \right]^2}. \quad (18)$$

Figure 12 depicts the vertical profiles of the aforementioned skill scores calculated for all coinciding observations without separating the different sites and time periods. The MDL value is within ± 0.12 for all altitudes, indicating that the retrieval is in very good agreement to the smoothed radiosonde data.

The scatter between GRUAN and IASI (σ_{MDL}) decreases slightly linearly with altitude starting at ± 0.3 at the ground and reaching ± 0.2 at 9 km. In contrast the variation of the smoothed radiosonde data, σ_{GRUAN} , reaches more than ± 0.5 in the lower troposphere and more than ± 1.0 in the middle and upper troposphere. This reflects the large variation in the atmospheric water vapour concentration data we use for our evaluation study (see also Fig. 2).

The small values of MDL and the small variations of σ_{MDL} throughout the atmosphere prove that the retrieval is able to detect the atmospheric water vapour concentration in all climate regions.

6 Summary

In this paper, we compare water vapour profiles retrieved from IASI spectra by the MUSICA MetOp/IASI retrieval with in situ measurements from GRUAN radiosondes at three different reference sites representative for three different climate zones (tropics, midlatitudes and polar region). Additionally we provide an extensive theoretical error estimation of the retrieval's water vapour product for the respective reference sites considering a large number of different uncertainty sources.

The error estimations of the MUSICA MetOp/IASI water vapour profiles at the different reference sites reveal that for the lowermost 3 km the errors can be as large as 40%. The most important uncertainty sources are unrecognized clouds and uncertainties in lower tropospheric temperature, in surface skin temperature, and in surface emissivity. Between 3 and 6 km the error can be as large as 20%, mainly due to middle atmospheric temperature uncertainties and unrecognized high cirrus clouds. Above 6 km the errors are typically smaller than 20% and mainly caused by uncertainties in upper tropospheric temperatures and uncertainties in spectroscopic pressure broadening parameters.

For the empirical validation study the remote sensing MUSICA MetOp/IASI H_2O profiles have been compared to 100 different Vaisala RS92 radiosonde measurements that have been processed by the GRUAN lead centre. The scatter found for the difference between GRUAN and IASI is smaller than 25% between 1.5 and 10 km altitude. It is slightly higher near the ground and close to the tropopause. This is in good agreement with errors as given for the GRUAN data and the errors as estimated for the MUSICA IASI product. It is important to note that the coincidences correspond to five different years and represent three different climate zones, giving the here presented study a good global representativeness. We demonstrate that the MUSICA MetOp/IASI retrieval is able to correctly capture variations in H_2O profiles between 1.5 km above ground up to the upper troposphere.



7 Data availability

The here presented MUSICA MetOp/IASI data are available on the MUSICA website <http://www.imk-asf.kit.edu/english/musica.php>. The structure of the data will be explained in a manuscript that is currently prepared for submission to Earth System Science Data (ESSD). In the meanwhile please contact M. Schneider for more details. The GRUAN data are available
5 at the GRUAN website: <https://www.gruan.org/data/data-products/gdp/rs92-gdp-2/>.



Appendix A: Uncertainties of GRUAN water vapour volume mixing ratios

In order to perform a valid comparison between remote sensing data and in situ measurements, the uncertainties of the in situ data have to be considered.

GRUAN provides uncertainties for the relative humidity ($\Delta\rho$), for the temperature (ΔT), and for the pressure (Δp). The water vapour volume mixing ratio (WVMR) is defined as

$$\text{WVMR} = \frac{\rho E(T)}{p - \rho E(T)} \approx \frac{\rho E(T)}{p}, \quad (\text{A1})$$

where E is the water vapour saturation pressure. The GRUAN WVMR error for each individual radiosonde can be calculated as

$$\text{WVMR}_e = \sqrt{\left(\frac{\Delta E(T)}{E(T)}\right)^2 + \left(\frac{\Delta\rho}{\rho}\right)^2} \times \text{WVMR}. \quad (\text{A2})$$

Uncertainties in atmospheric pressure p can be neglected if compared to the uncertainties of $E(T)$ and ρ . For the calculation of the water vapour saturation pressure we use the same formula as GRUAN from Hyland and Wexler (1983). Since $E(T)$ is a highly non-linear function, we estimate the uncertainty of E by

$$\Delta E = \max\{|E(T + \Delta T) - E(T)|; |E(T - \Delta T) - E(T)|\}. \quad (\text{A3})$$

According to Dirksen et al. (2014) there are correlated and uncorrelated errors. We investigate both separately. Figure A1 depicts for the correlated and uncorrelated GRUAN WVMR errors (WVMR_e) in the top and bottom panels, respectively. Black lines indicate the data ensembles that cover all seasons (Manus Island and Lindenberg 2008) and red lines the ensembles that are only representative for the summer season (Lindenberg 2007 and Sodankylä).

For a reasonable comparison the vertically high resolved GRUAN profiles have to be adjusted to the vertical resolution of the remote sensing profiles (see Sect. 5.1). This means a significant reduction of the vertical resolution and the uncorrelated errors will cancel out. The regridding and smoothing of the uncorrelated errors is accomplished as follows: First, the errors WVMR_e are added to the measured WVMR data. Second, for $\text{WVMR} + \text{WVMR}_e$ we perform the regridding as described in Sect. 5.1, i.e. we calculate the regridded version of the erroneous GRUAN WVMR profile. The difference between the erroneous and the original profiles (of the regridded versions) give the regridded GRUAN WVMR error (ϵ_{GRUAN}). Third, in analogy to Eq. (13) we apply the averaging kernels to ϵ_{GRUAN} and get the error in the regridded and smoothed GRUAN profiles as:

$$\hat{\mathbf{x}}_{e,\text{GRUAN}} = (\mathbf{A}_{11} + \mathbf{A}_{12})\epsilon_{\text{GRUAN}}. \quad (\text{A4})$$

Figure A2 depicts these error profiles ($\hat{\mathbf{x}}_{e,\text{GRUAN}}$) for the different ensembles. The uncertainties typically increase from 5% near the ground to values 5-20% at around 10 km altitude. For higher altitudes it decreases again due to the decaying sensitivity (see averaging kernel plots of Fig. 3).



Author contributions. C. Borger performed most calculations for this work during his master thesis at KIT IMK-ASF and prepared the manuscript in collaboration with all coauthors. M. Schneider developed the MetOp/IASI retrievals in the framework of the MUSICA project and B. Ertl supported these developments by making the processing chain more efficiently. F. Hase wrote the PROFFIT and PRFFWD codes. O. García helped in reading and formatting the EUMETSAT IASI L2 data. M. Sommer provided the GRUAN radiosonde measurements in a very useful data format for the sites of Lindenberg and Sodankylä. M. Höpfner helped us with the KOPRA calculations used for estimating the effect of the scattering by cirrus and mineral dust particles. S. Tjemkes provided all necessary data for the site of Manus Island in a very useful data format in the framework of a planned exercise called “Intercomparison of Hyperspectral Retrieval Codes”. X. Calbet collected the IASI/GRUAN coincidences over Manus Island and helped us in the interpretation of the radiosonde’s measurement uncertainties.

Acknowledgements. This research has largely benefit from results of the projects MUSICA (funded by the European Research Council under the European Community’s Seventh Framework Programme (FP7/2007-2013) / ERC Grant agreement number 256961), MOTIV (funded by the Deutsche Forschungsgemeinschaft under GZ SCHN 1126/2-1) and INMENSE (funded by the Ministerio de Economía y Competividad from Spain, CGL2016-80688-P). We acknowledge the support by the Deutsche Forschungsgemeinschaft and the Open Access Publishing Fund of the Karlsruhe Institute of Technology.

15





References

- August, T., Klaes, D., Schluessel, P., Hultberg, T., Crapeau, M., Arriaga, A., O'Carroll, A., Coppens, D., Munro, R., and Calbet, X.: IASI on Metop-A: Operational Level 2 retrievals after five years in orbit, 113, 1340–1371, 2012.
- Barthlott, S., Schneider, M., Hase, F., Blumenstock, T., Kiel, M., Dubravica, D., García, O. E., Sepúlveda, E., Mengistu Tsidu, G., Takele Ke-
5 nea, S., Grutter, M., Plaza-Medina, E. F., Stremme, W., Strong, K., Weaver, D., Palm, M., Warneke, T., Notholt, J., Mahieu, E., Servais, C., Jones, N., Griffith, D. W. T., Smale, D., and Robinson, J.: Tropospheric water vapour isotopologue data (H_2^{16}O , H_2^{18}O , and HD^{16}O) as obtained from NDACC/FTIR solar absorption spectra, *Earth System Science Data*, 9, 15–29, <https://doi.org/10.5194/essd-9-15-2017>, <http://www.earth-syst-sci-data.net/9/15/2017/>, 2017.
- Calbet, X., Kivi, R., Tjemkes, S., Montagner, F., and Stuhlmann, R.: Matching radiative transfer models and radiosonde
10 data from the EPS/Metop Sodankylä campaign to IASI measurements, *Atmospheric Measurement Techniques*, 4, 1177–1189, <https://doi.org/10.5194/amt-4-1177-2011>, <http://www.atmos-meas-tech.net/4/1177/2011/>, 2011.
- Calbet, X., Peinado-Galan, N., Rípodas, P., Trent, T., Dirksen, R., and Sommer, M.: Consistency between GRUAN sondes, LBLRTM and IASI, *Atmospheric Measurement Techniques*, 10, 2323–2335, <https://doi.org/10.5194/amt-10-2323-2017>, <https://www.atmos-meas-tech.net/10/2323/2017/>, 2017.
- 15 Clerbaux, C., Boynard, A., Clarisse, L., George, M., Hadji-Lazaro, J., Herbin, H., Hurtmans, D., Pommier, M., Razavi, A., Turquety, S., Wespes, C., and Coheur, P.-F.: Monitoring of atmospheric composition using the thermal infrared IASI/MetOp sounder, *Atmos. Chem. Phys.*, 9, 6041–6054, 2009.
- Delamere, J. S., Clough, S. A., Payne, V. H., Mlawer, E. J., Turner, D. D., and Gamache, R. R.: A far-infrared radiative closure study in the Arctic: Application to water vapor, *Journal of Geophysical Research: Atmospheres*, 115, n/a–n/a, <https://doi.org/10.1029/2009JD012968>,
20 <http://dx.doi.org/10.1029/2009JD012968>, d17106, 2010.
- Dirksen, R. J., Sommer, M., Immler, F. J., Hurst, D. F., Kivi, R., and Vömel, H.: Reference quality upper-air measurements: GRUAN data processing for the Vaisala RS92 radiosonde, *Atmospheric Measurement Techniques*, 7, 4463–4490, <https://doi.org/10.5194/amt-7-4463-2014>, <http://www.atmos-meas-tech.net/7/4463/2014/>, 2014.
- Gao, B.-C. and Kaufman, Y. J.: Water vapor retrievals using Moderate Resolution Imaging Spectroradiometer (MODIS) near-infrared chan-
25 nels, *Journal of Geophysical Research: Atmospheres*, 108, n/a–n/a, <https://doi.org/10.1029/2002JD003023>, <http://dx.doi.org/10.1029/2002JD003023>, 4389, 2003.
- García, O. E., Sepúlveda, E., Schneider, M., Wiegeler, A., Borger, C., Hase, F., Barthlott, S., Blumenstock, T., and de Frutos, A. M.: Upper tropospheric CH_4 and N_2O retrievals from MetOp/IASI within the project MUSICA, *Atmospheric Measurement Techniques Discussions*, 2017, 1–32, <https://doi.org/10.5194/amt-2016-326>, <http://www.atmos-meas-tech-discuss.net/amt-2016-326/>, 2017.
- 30 Gordon, I., Rothman, L., Hill, C., Kochanov, R., Tan, Y., Bernath, P., Birk, M., Boudon, V., Campargue, A., Chance, K., Drouin, B., Flaud, J.-M., Gamache, R., Hodges, J., Jacquemart, D., Perevalov, V., Perrin, A., Shine, K., Smith, M.-A., Tennyson, J., Toon, G., Tran, H., Tyuterev, V., Barbe, A., Császár, A., Devi, V., Furtenbacher, T., Harrison, J., Hartmann, J.-M., Jolly, A., Johnson, T., Karman, T., Kleiner, I., Kyuberis, A., Loos, J., Lyulin, O., Massie, S., Mikhailenko, S., Moazzen-Ahmadi, N., Müller, H., Naumenko, O., Nikitin, A., Polyansky, O., Rey, M., Rotger, M., Sharpe, S., Sung, K., Starikova, E., Tashkun, S., Auwera, J. V., Wagner, G., Wilzewski, J., Weislo, P.,
35 Yu, S., and Zak, E.: The HITRAN2016 molecular spectroscopic database, *Journal of Quantitative Spectroscopy and Radiative Transfer*, <https://doi.org/https://doi.org/10.1016/j.jqsrt.2017.06.038>, <http://www.sciencedirect.com/science/article/pii/S0022407317301073>, 2017.



- Grossi, M., Valks, P., Loyola, D., Aberle, B., Slijkhuis, S., Wagner, T., Beirle, S., and Lang, R.: Total column water vapour measurements from GOME-2 MetOp-A and MetOp-B, *Atmospheric Measurement Techniques*, 8, 1111–1133, <https://doi.org/10.5194/amt-8-1111-2015>, <http://www.atmos-meas-tech.net/8/1111/2015/>, 2015.
- Hase, F., Hannigan, J. W., Coffey, M. T., Goldman, A., Höpfner, M., Jones, N. B., Rinsland, C. P., and Wood, S.: Intercomparison of retrieval codes used for the analysis of high-resolution, *J. Quant. Spectrosc. Ra.*, 87, 25–52, 2004.
- Herbin, H., Hurtmans, D., Clerbaux, C., Clarisse, L., and Coheur, P.-F.: H_2^{16}O and HDO measurements with IASI/MetOp, *Atmos. Chem. Phys.*, 9, 9433–9447, 2009.
- Hess, M., Koepke, P., and Schult, I.: Optical Properties of Aerosols and Clouds: The Software Package OPAC, *Bulletin of the American Meteorological Society*, 79, 831–844, [https://doi.org/10.1175/1520-0477\(1998\)079<0831:OPOAAC>2.0.CO;2](https://doi.org/10.1175/1520-0477(1998)079<0831:OPOAAC>2.0.CO;2), [http://dx.doi.org/10.1175/1520-0477\(1998\)079<0831:OPOAAC>2.0.CO;2](http://dx.doi.org/10.1175/1520-0477(1998)079<0831:OPOAAC>2.0.CO;2), 1998.
- Hyland, R. and Wexler, A.: Formulations for the thermodynamic properties of the saturated phases of H₂O from 173.15 K to 473.15 K, *ASHRAE transactions*, 89, 500–519, 1983.
- Koepke, P., Gasteiger, J., and Hess, M.: Technical Note: Optical properties of desert aerosol with non-spherical mineral particles: data incorporated to OPAC, *Atmospheric Chemistry and Physics*, 15, 5947–5956, <https://doi.org/10.5194/acp-15-5947-2015>, <http://www.atmos-chem-phys.net/15/5947/2015/>, 2015.
- Masuda, K., Takashima, T., and Takayama, Y.: Emissivity of pure and sea waters for the model sea surface in the infrared window regions, *Remote Sensing of Environment*, 24, 313 – 329, [https://doi.org/http://dx.doi.org/10.1016/0034-4257\(88\)90032-6](https://doi.org/http://dx.doi.org/10.1016/0034-4257(88)90032-6), <http://www.sciencedirect.com/science/article/pii/0034425788900326>, 1988.
- Mlawer, E. J., Payne, V. H., Moncet, J.-L., Delamere, J. S., Alvarado, M. J., and Tobin, D. C.: Development and recent evaluation of the MT_CKD model of continuum absorption, *Philosophical Transactions of the Royal Society of London A: Mathematical, Physical and Engineering Sciences*, 370, 2520–2556, <https://doi.org/10.1098/rsta.2011.0295>, 2012.
- Payne, V. H., Mlawer, E. J., Cady-Pereira, K. E., and Moncet, J. L.: Water Vapor Continuum Absorption in the Microwave, *IEEE Transactions on Geoscience and Remote Sensing*, 49, 2194–2208, <https://doi.org/10.1109/TGRS.2010.2091416>, 2011.
- Pequignot, E., Blumstein, D., and Larigauderie, C.: CNES Technical Note: IASI Noise Covariance Matrix, Tech. rep., IA-TN-0000-3271-CNE, 2008.
- Pougatchev, N., August, T., Calbet, X., Hultberg, T., Oduleye, O., Schlüssel, P., Stiller, B., Germain, K. S., and Bingham, G.: IASI temperature and water vapor retrievals – error assessment and validation, *Atmospheric Chemistry and Physics*, 9, 6453–6458, <https://doi.org/10.5194/acp-9-6453-2009>, <https://www.atmos-chem-phys.net/9/6453/2009/>, 2009.
- Rodgers, C.: *Inverse Methods for Atmospheric Sounding: Theory and Praxis*, World Scientific Publishing Co., Singapore, 2000.
- Rosenkranz, P. W.: Retrieval of water vapor from AMSU-A and AMSU-B measurements, in: *IGARSS 2000. IEEE 2000 International Geoscience and Remote Sensing Symposium. Taking the Pulse of the Planet: The Role of Remote Sensing in Managing the Environment. Proceedings (Cat. No.00CH37120)*, vol. 7, pp. 3033–3035 vol.7, <https://doi.org/10.1109/IGARSS.2000.860326>, 2000.
- Schneider, M. and Hase, F.: Optimal estimation of tropospheric H₂O and δD with IASI/METOP, *Atmos. Chem. Phys.*, 11, 11 207–11 220, <https://doi.org/10.5194/acp-11-11207-2011>, 2011.
- Schneider, M., Wiegeler, A., Barthlott, S., González, Y., Christner, E., Dyroff, C., García, O. E., Hase, F., Blumenstock, T., Sepúlveda, E., Mengistu Tsidu, G., Takele Kenea, S., Rodríguez, S., and Andrey, J.: Accomplishments of the MUSICA project to provide accurate, long-term, global and high-resolution observations of tropospheric {H₂O, δD } pairs – a review, *Atmospheric Measurement Techniques*, 9, 2845–2875, <https://doi.org/10.5194/amt-9-2845-2016>, <http://www.atmos-meas-tech.net/9/2845/2016/>, 2016.



- Seemann, S. W., Borbas, E. E., Knuteson, R. O., Stephenson, G. R., and Huang, H.-L.: Development of a Global Infrared Land Surface Emissivity Database for Application to Clear Sky Sounding Retrievals from Multispectral Satellite Radiance Measurements, *Journal of Applied Meteorology and Climatology*, 47, 108–123, <https://doi.org/10.1175/2007JAMC1590.1>, <http://dx.doi.org/10.1175/2007JAMC1590.1>, 2008.
- 5 Sommer, M., Dirksen, R., and von Rohden, C.: Brief Description of the RS92 GRUAN Data Product (RS92-GDP), GRUAN-TD-4, Tech. rep., GRUAN Lead Centre, <https://www.gruan.org/documentation/gruan/td/gruan-td-4/>, version 2, 2016.
- Stevens, B. and Bony, S.: What Are Climate Models Missing?, *Science*, 340, 1053–1054, <https://doi.org/10.1126/science.1237554>, <http://www.sciencemag.org/content/340/6136/1053.short>, 2013.
- Stiller, G.: The Karlsruhe optimized and precise radiative transfer algorithm (KOPRA), Tech. rep., Karlsruhe, wissenschaftliche Berichte /
- 10 Forschungszentrum Karlsruhe in der Helmholtz-Gemeinschaft, FZKA ; 6487, 2000.
- Wiegele, A., Schneider, M., Hase, F., Barthlott, S., García, O. E., Sepúlveda, E., González, Y., Blumenstock, T., Raffalski, U., Gisi, M., and Kohlhepp, R.: The MUSICA MetOp/IASI H₂O and dD products: characterisation and long-term comparison to NDACC/FTIR data, *Atmospheric Measurement Techniques*, 7, 2719–2732, <https://doi.org/10.5194/amt-7-2719-2014>, <http://www.atmos-meas-tech.net/7/2719/2014/>, 2014.
- 15 Worden, J., Kulawik, S., Frankenberg, C., Payne, V., Bowman, K., Cady-Peirara, K., Wecht, K., Lee, J.-E., and Noone, D.: Profiles of CH₄, HDO, H₂O, and N₂O with improved lower tropospheric vertical resolution from Aura TES radiances, *Atmospheric Measurement Techniques*, 5, 397–411, <https://doi.org/10.5194/amt-5-397-2012>, <http://www.atmos-meas-tech.net/5/397/2012/>, 2012.
- Zhang, J., Chen, H., Li, Z., Fan, X., Peng, L., Yu, Y., and Cribb, M.: Analysis of cloud layer structure in Shouxian, China using RS92 radiosonde aided by 95 GHz cloud radar, *Journal of Geophysical Research: Atmospheres*, 115, n/a–n/a,
- 20 <https://doi.org/10.1029/2010JD014030>, <http://dx.doi.org/10.1029/2010JD014030>, d00K30, 2010.

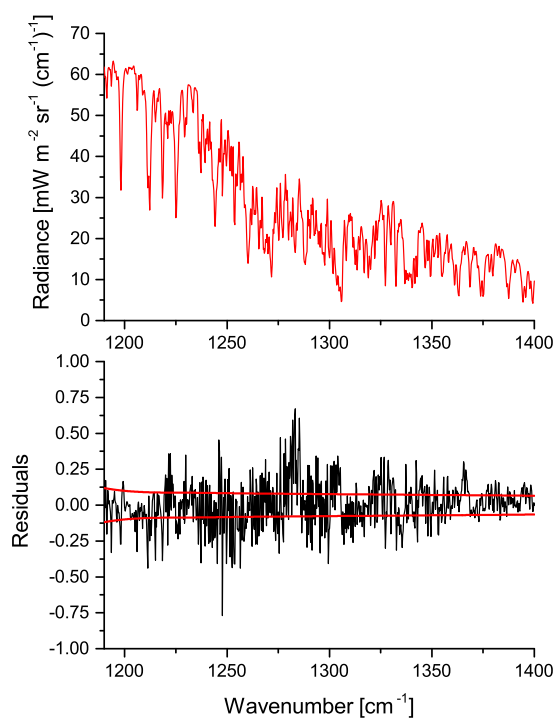


Figure 1. Example of an infrared spectra measured by IASI (upper panel) and residuals between satellite observation and radiative transfer simulation (bottom panel) at Manus Island (2012-10-15 11:46:26 UT, satellite zenith angle 10.16°, integrated water vapour 59.49 kg m⁻²). The red lines in the bottom panel indicate the typical IASI noise measurement level as given by the square root values of the diagonal elements of the IASI noise covariance matrix (Pequignot et al., 2008).

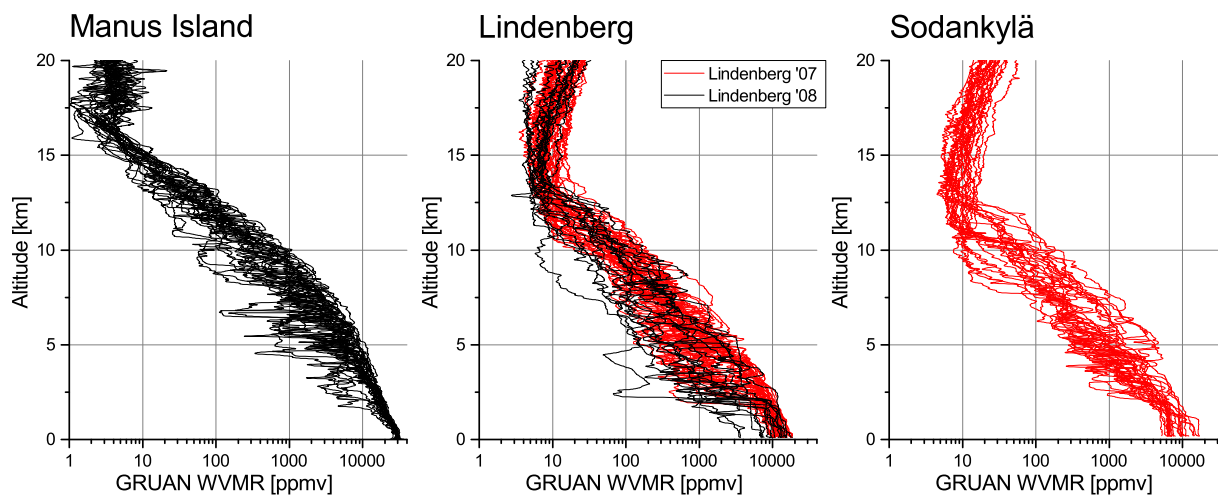


Figure 2. Vertical H₂O profiles as measured by the 100 different GRUAN processed Vaisala RS92 radiosondes: from Manus Island, Lindenberg and Sodankylä used for our study. Black lines indicate radiosonde data ensembles that cover all seasons (Manus Island and Lindenberg 2008) and red lines indicate ensembles that cover the summer season only.

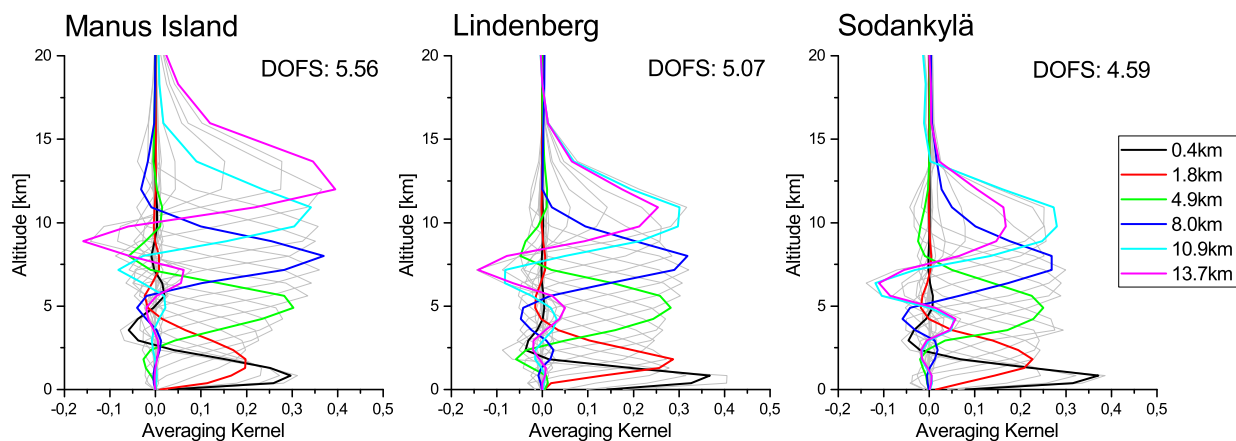


Figure 3. Example row kernels ($\mathbf{A}_{11} + \mathbf{A}_{12}$, see Eq. 11) for the three reference sites. Manus Island: 2013-11-28 11:39:14 UT, satellite zenith angle 12.44° , integrated water vapour 55.75 kg m^{-2} ; Lindenberg: 2008-06-03 08:59:14 UT, 23.95° , 20.05 kg m^{-2} ; Sodankylä: 2007-06-07 18:40:38 UT, 17.70° , 11.17 kg m^{-2} . Numbers in the upper right corners of every panel indicate the respective degrees of freedom of signal (DOFS).

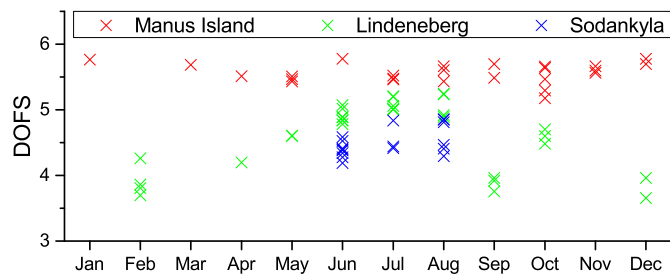


Figure 4. Variation of the DOFS values (degree of freedom for signal) for the three reference sites.

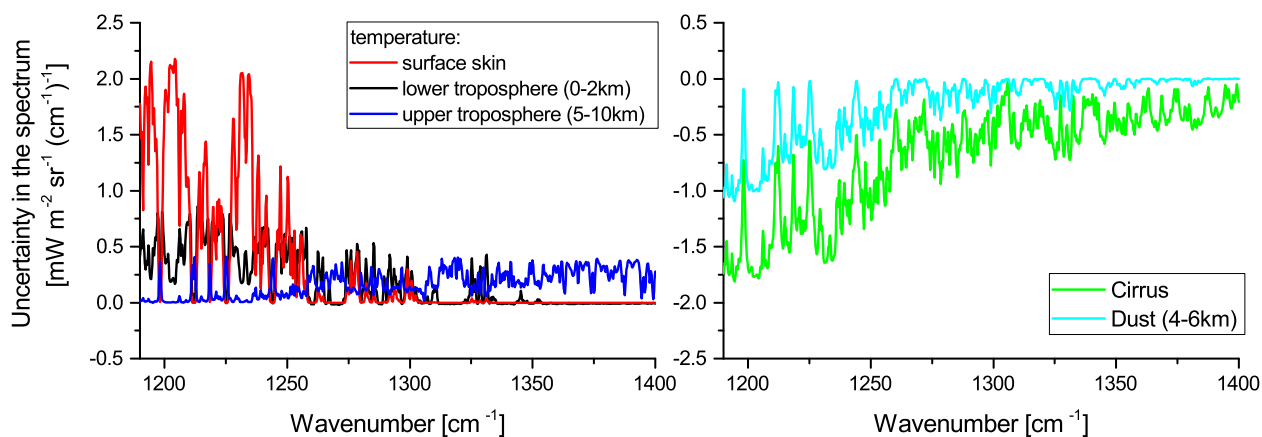


Figure 5. Spectral responses of uncertainty sources for a typical situation at Manus Island (same situation as for the kernel in Fig. 3). The left panel shows examples for the influence of uncertainties in temperatures (surface skin $\Delta T = +2$ K, lower tropospheric $\Delta T = +2$ K and upper tropospheric $\Delta T = +1$ K). The right panel illustrates examples for the influence of clouds (dust layer (4-6 km) and cirrus cloud (13-14 km and 50% cloud fraction)) on the spectrum. Please note the different y-axis scales, i.e. the positive response for positive temperature uncertainties and the negative response for unrecognized clouds.

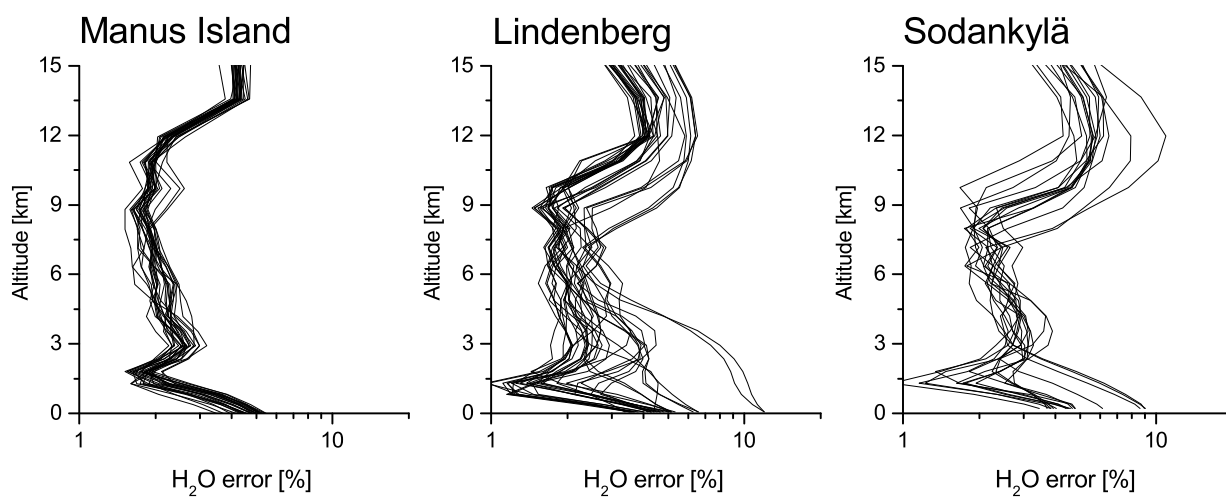


Figure 6. H₂O error profiles caused by instrument noise calculated as the square root value of the diagonal of the matrix S_e according to Eq. (9). Shown are the error profiles for every situation examined in the validation study.

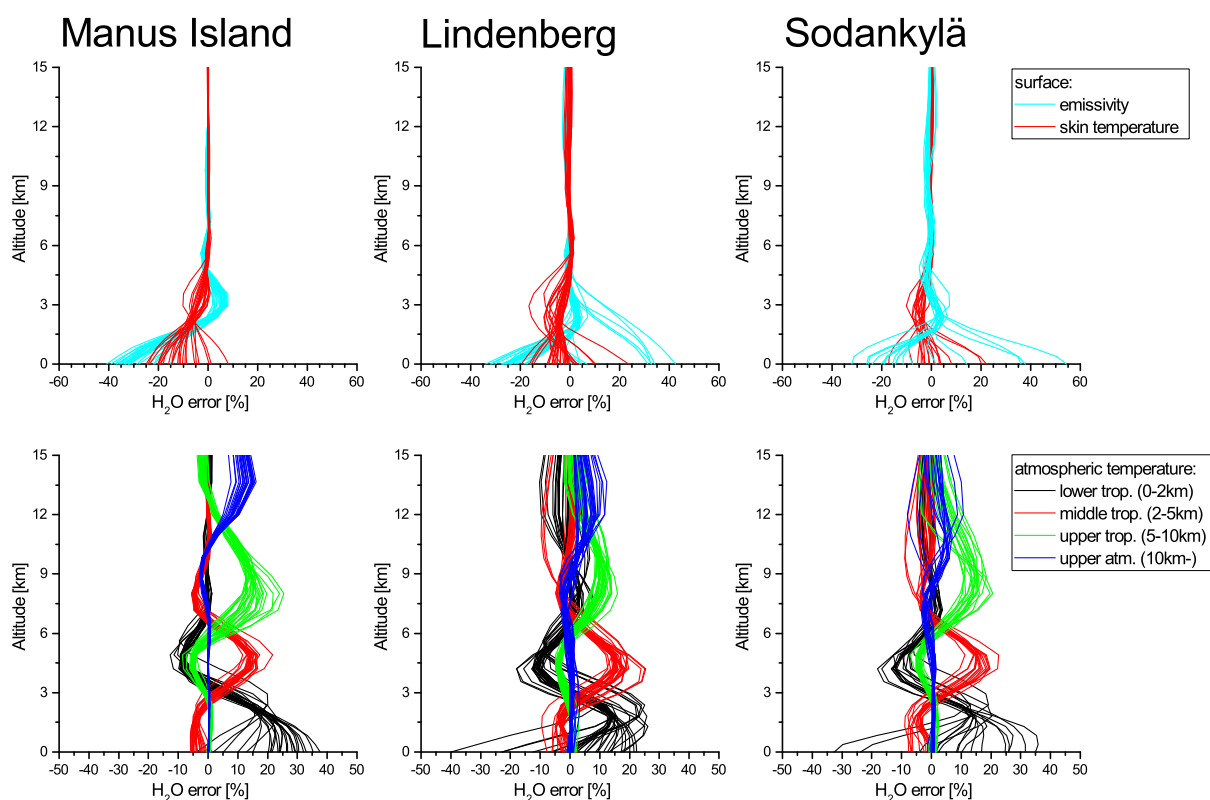


Figure 7. H₂O error pattern profiles x_e according to Eq. (7) due to uncertainties in surface properties (skin temperature and emissivity) and atmospheric air temperature (lower tropospheric, mid tropospheric, upper tropospheric and upper atmospheric) at the 3 different reference sites. Shown are the error patterns for every situation examined in the validation study.

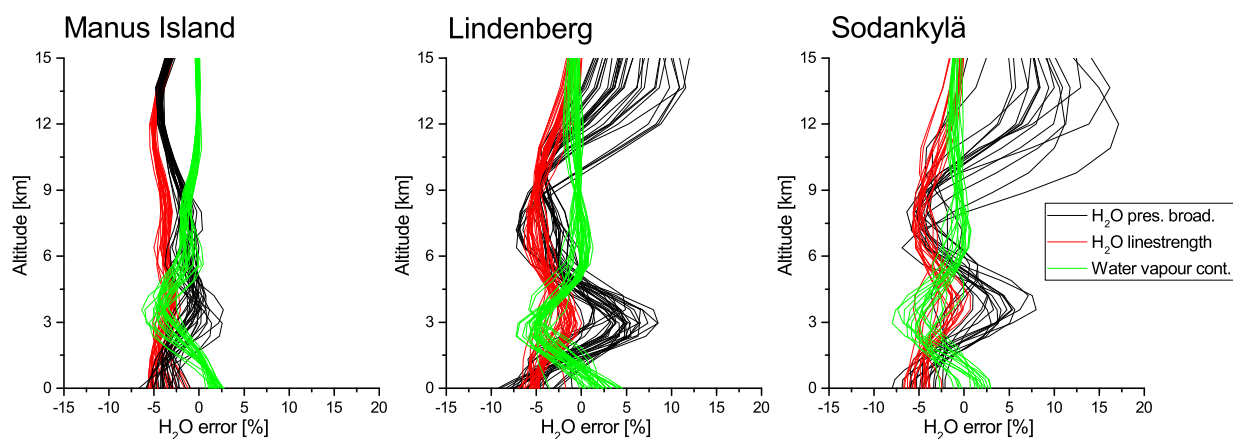


Figure 8. Same as Fig. 7, but for errors due to uncertainties in the H₂O spectroscopic parameters (linestrength, +5%, and pressure broadening, +5%) and the water vapour continuum (assuming a 10% underestimation of the “MT_CKD” model).

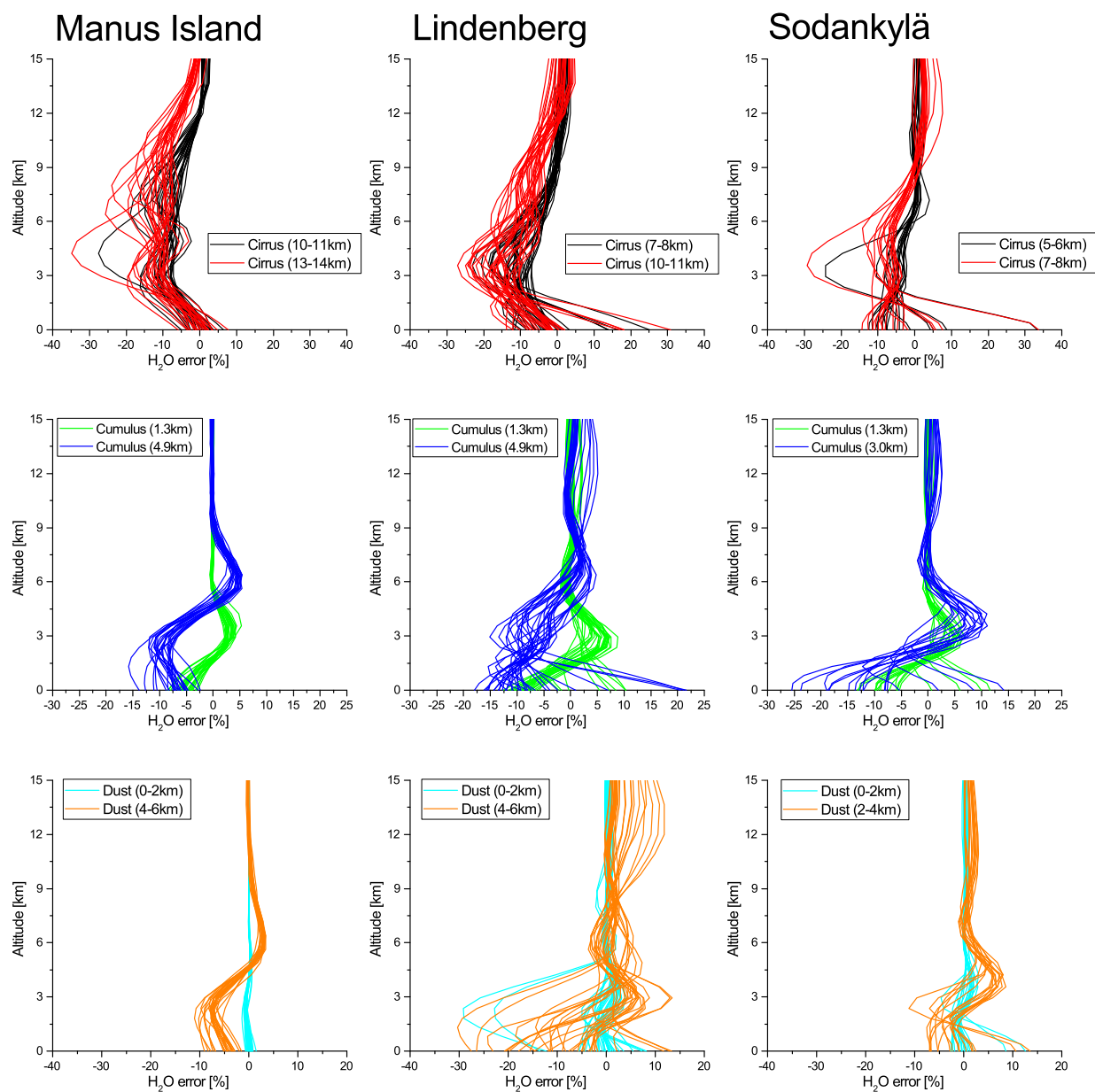


Figure 9. Same as Fig. 7, but for errors due to unrecognized clouds (cirrus, mineral dust, cumulus). Top panels: cirrus clouds with 50% fractional coverage located at typical middle/upper tropospheric altitudes (location of cloud layers see legend); Middle panels: cumulus clouds with 10% fractional coverage with cloud top altitudes as given in the legends; Bottom panel: homogeneous dust clouds with layers as given in the legends.

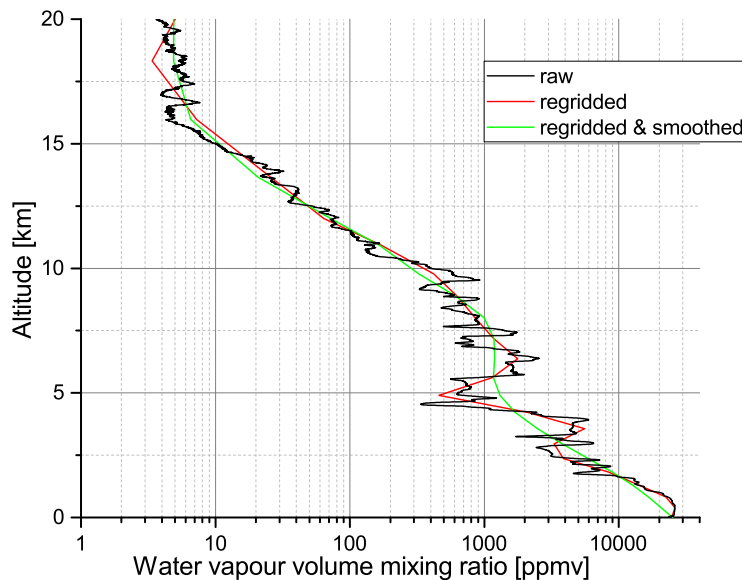


Figure 10. Example for the regridding and smoothing of the GRUAN data required before validating the MUSICA MetOp/IASI retrieval H_2O profiles. Black line: raw GRUAN data; Red line: regridded GRUAN data (x_{GRUAN}); Green line: regridded and smoothed radiosonde data (\hat{x}_{GRUAN} , according to Eq. 13).

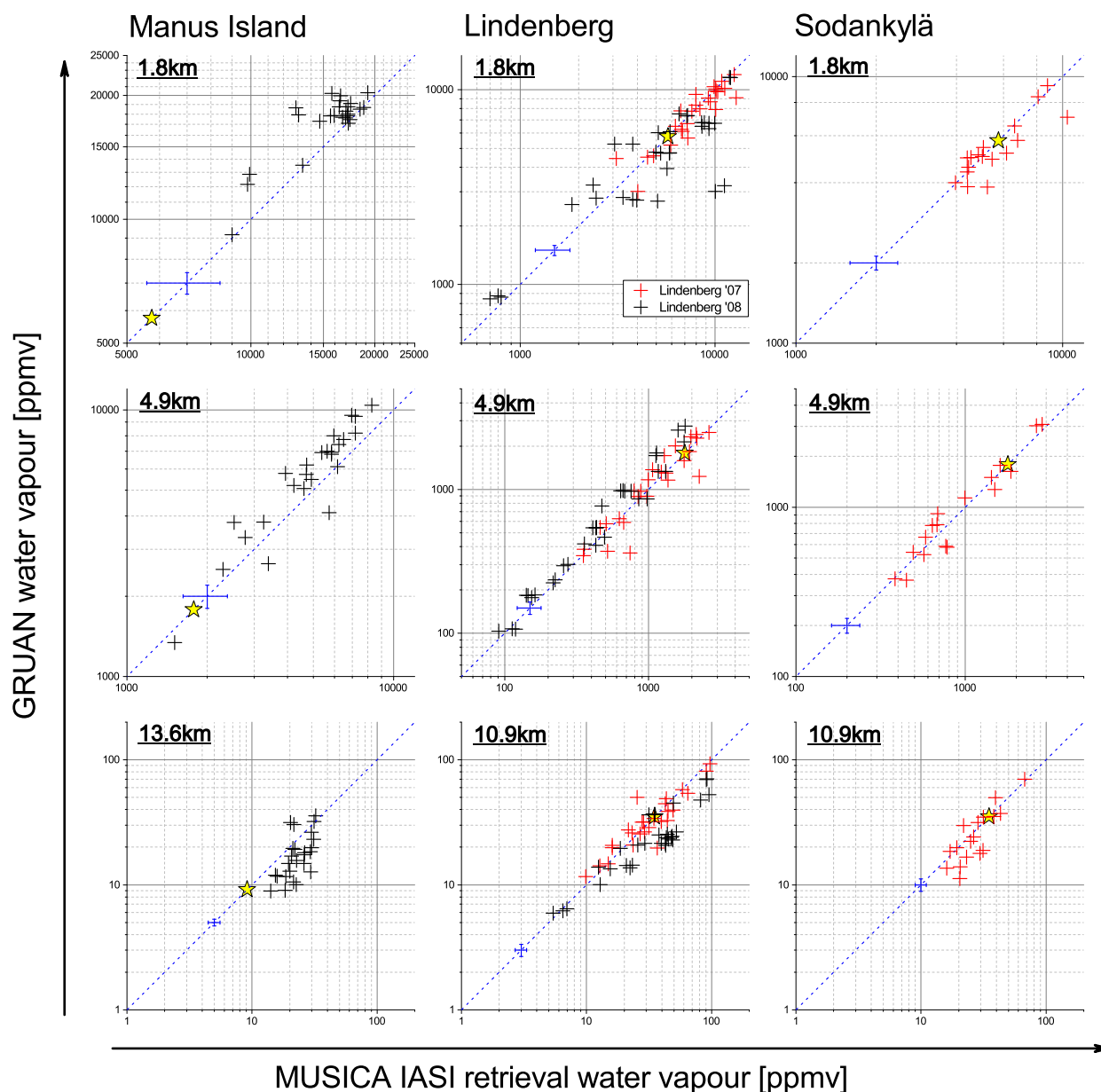


Figure 11. Correlation between GRUAN (along y-axes) and MUSICA MetOp/IASI data (along x-axes) at the 3 different reference sites for 3 different atmospheric levels (lower, middle and upper troposphere). The yellow star represents the a priori assumption for the respective retrieval level (the retrieval uses globally the same a priori). The respective retrieval level altitudes are given in the individual scatter plots. Red and black colour distinguish the remote sensing data ensembles that use different input data (MI and LI08, on the one hand, and LI07 and SK07, on the other hand; see Sect. 3.1 and Tab. 1). The blue dotted line represents the 1-to-1 diagonal and the blue error bars indicate the typical GRAUN and IASI errors.

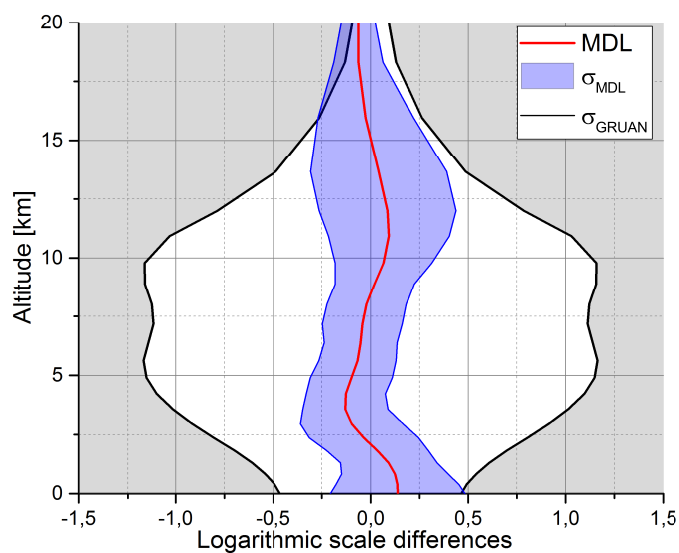


Figure 12. Vertical profiles of retrieval skill scores calculated according to Eqs. (16)-(18) and using data from all ensembles (MI, LI07, LI08 and SK07). MDL (red line) is the mean difference between IASI and smoothed GRUAN data; $\pm\sigma_{\text{MDL}}$ (blue lines and blue shaded area) is the 1σ scatter between IASI and smoothed GRUAN data; $\pm\sigma_{\text{GRUAN}}$ (black lines) is the 1σ variability of smoothed GRUAN data.

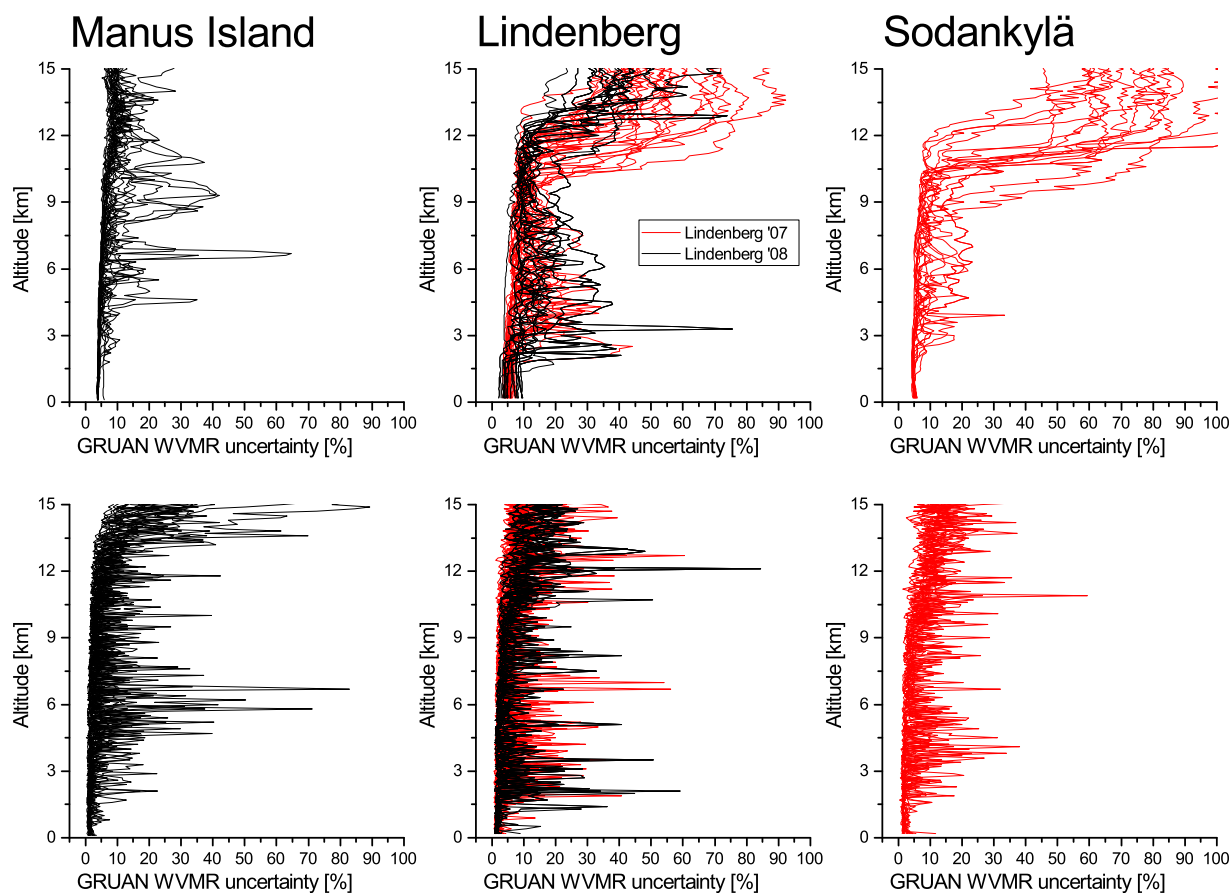


Figure A1. Profiles of the WVMR errors of the GRUAN radiosondes: The top panels represent the correlated errors and the bottom panels the uncorrelated errors. The colours distinguish the different ensembles of the retrieval setup: black for MI and LI08, red for LI07 and SK07.

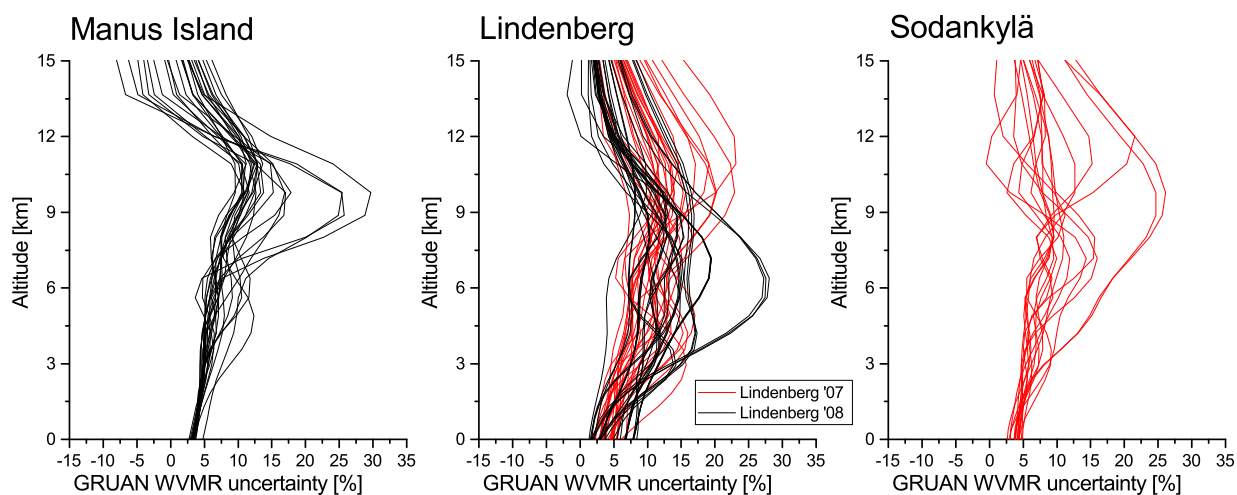


Figure A2. Same as top panels of Fig. A1, but for the correlated errors in the regridded and smoothed GRUAN radiosonde data.



Table 1. Overview of the reference and retrieval input data sets

	Manus Island	Lindenberg 2008	Lindenberg 2007	Sodankylä 2007
time period	2011-2013	2008 (all months)	2007 (June, July, August)	2007 (June, July, August)
ground level	IASI L2 (GTOPO30)	IASI L2 (GTOPO30)	GTOPO30	GTOPO30
emissivity	IASI L2 (Masuda et al., 1988)	IASI L2 (IREMIS)	IREMIS	IREMIS
cloud identification	IASI L2, visual inspection	IASI L2	Zhang et al. (2010)	Zhang et al. (2010)
a priori for atmospheric and surface skin temperature	IASI L2	IASI L2	Radiosonde	Radiosonde
number of GRUAN sondes	25	32	26	17

**Table 2.** List of uncertainty assumptions used for the error estimation of the MUSICA MetOp/IASI water vapour product

uncertainty source	uncertainty value
Surface emissivity	2%
Surface skin temperature	2 K
Temperature in lower troposphere (0-2 km)	2 K
Temperature in middle troposphere (2-5 km)	1 K
Temperature in upper troposphere (5-10 km)	1 K
Temperature in upper atmosphere (10 km-)	1 K
Water vapour continuum	10% of model MT_CKD v2.5.2
Line intensity H ₂ O	5%
Pressure-broadening H ₂ O	5%
Line intensity HDO	5%
Pressure-broadening HDO	5%
CH ₄ concentrations	2%
N ₂ O concentrations	2%
Opaque cumulus cloud	10% fractional cover with cloud top at 1.3, 3.0 and 4.9 km
Cirrus cloud	particle properties according to OPAC "Cirrus 3", 1 km thickness, 50% fractional cover with cloud top at 6, 8, 11 and 14 km
Mineral dust cloud	particle properties according to OPAC "Desert", homogeneous coverage for layers: ground-2 km, 2-4 km and 4-6 km